

High-order dynamic localization and tunable temporal cloaking in ac-electric-field driven synthetic lattices

Shulin Wang

Huazhong University of Science and Technology

Chengzhi Qin

Huazhong University of Science and Technology

Weiwei Liu

Huazhong University of Science and Technology <https://orcid.org/0000-0001-9451-1968>

Bing Wang (✉ wangbing@hust.edu.cn)

Huazhong University of Science and Technology

Feng Zhou

Han Ye

Huazhong University of Science and Technology

Lange Zhao

Huazhong University of Science and Technology

Jianji Dong

Wuhan National Laboratory for Optoelectronics, School of Optical and Electronic Information, Huazhong University of Science and Technology, Wuhan 430074

Xinliang Zhang

Wuhan National Laboratory for Optoelectronics, Huazhong University of Science and Technology, Wuhan, 430074

Stefano Longhi

Politecnico di Milano

Peixiang Lu

Huazhong University of Science and Technology <https://orcid.org/0000-0001-6993-8986>

Article

Keywords:

Posted Date: April 8th, 2022

DOI: <https://doi.org/10.21203/rs.3.rs-1457419/v1>

License: © ⓘ This work is licensed under a Creative Commons Attribution 4.0 International License.

[Read Full License](#)

High-order dynamic localization and tunable temporal cloaking in ac-electric-field driven synthetic lattices

Shulin Wang^{1,2,#}, Chengzhi Qin^{1,2,#}, Weiwei Liu^{1,2,#}, Bing Wang^{1,2,*}, Feng Zhou^{1,2}, Han Ye^{1,2}, Lange Zhao^{1,2}, Jianji Dong^{1,2}, Xinliang Zhang^{1,2}, Stefano Longhi^{4,5,*}, and Peixiang Lu^{1,2,3,*}

¹Wuhan National Laboratory for Optoelectronics and School of Physics, Huazhong University of Science and Technology, Wuhan 430074, China.

²Optics Valley Laboratory, Hubei 430074, China.

³Hubei Key Laboratory of Optical Information and Pattern Recognition, Wuhan Institute of Technology, Wuhan 430205, China.

⁴Dipartimento di Fisica, Politecnico di Milano, Piazza Leonardo da Vinci 32, I-20133 Milano, Italy.

⁵IFISC (UIB-CSIC), Instituto de Física Interdisciplinar y Sistemas Complejos, E-07122 Palma de Mallorca, Spain.

[#]These authors contributed equally to this work

*Corresponding authors:

B. W. (email: wangbing@hust.edu.cn),

S. L. (email: stefano.longhi@polimi.it),

P. L. (email: lupeixiang@hust.edu.cn).

Abstract

Dynamic localization (DL) of photons, i.e., the light-motion cancellation effect arising from lattice's quasi-energy band collapse under a synthetic ac-electric-field, provides a powerful and alternative mechanism to Anderson localization for coherent light confinement. So far only low-order DLs, corresponding to weak ac-fields, have been demonstrated using curved-waveguide lattices where the waveguide's bending curvature plays the role of ac-field as required in original Dunlap-Kenkre model of DL. However, the inevitable bending losses pose a severe limitation for the observation of high-order DL. Here, we break the weak-field limitation by transferring lattice concepts from spatial to synthetic time dimensions using fiber-loop circuits and observe up to fifth-order DL. We find that high-order DLs possess superior localization and robustness against random noise over lower-order ones. As an exciting application, by judiciously combining low- and high-order DLs, we demonstrate a temporal cloaking scheme with flexible tunability both for cloak's window size and opening time. Our work pushes DL towards high-order regimes using synthetic-lattice schemes, which may find potential applications in robust signal transmission, protection, processing and cloaking.

Introduction

Application of an electric field in solids gives rise to a series of coherent transport effects for electrons, ranging from dc electric-field driven Bloch oscillations^{1,2} and Landau-Zener tunneling^{3,4} to ac electric-field driven dynamic localization (DL)⁵⁻⁷. DL refers to a wave-motion cancellation phenomenon of electron wave packet subject to an ac electric field at some magic values of the amplitude-to-frequency ratio. Such a localization mechanism stems from the quasi-energy band collapse of the ac-driven lattice⁶ and provides an efficient approach for coherent light confinement, as highly alternative to the well-known Anderson localization that relies on disordered or quasi-periodic potentials⁸⁻¹⁰. The simplest case of DL was introduced by Dunlap and Kenkre more than three decades ago for an electron hopping on a tight-binding lattice with nearest-neighbor hopping driven by an harmonic electric field⁵, where quasi-energy band collapse is achieved⁶ as the field's amplitude-to-frequency ratio takes a series of Bessel function's roots, which are termed as different orders of DLs. The curved optical waveguide array system has provided a powerful setting to realize the Dunlap-Kenkre model of DL for photons¹¹⁻¹⁵, as well as other DL regimes¹⁶⁻¹⁸. Likewise, DL can arise in time-modulated resonator arrays^{19,20}, with applications in optical switching, filtering, and beam reshaping. However, so far only the first and second orders of DLs have been experimentally achieved in the curved waveguide array setup^{11,12}, limited by the considerable bending losses in highly curved arrays. DLs at high-order regimes may be desirable, since they enhance the wave-packet localization strength and increase light-matter interaction.

Recently, the concepts of synthetic dimensions have emerged as ideal platforms for exploring various light transport behaviors, such as in time²¹⁻³¹, frequency³²⁻³⁶ and orbital angular momentum³⁷⁻⁴⁰ spaces. Benefit from their intrinsic conveniences of control with external modulations, numerous fundamental physical concepts that are difficult to demonstrate in spatial lattices have been realized in synthetic dimensions, ranging from parity-time symmetry²³, the topological invariant's measurement³⁹, topological band windings³⁴⁻³⁶ to non-Hermitian skin effect²⁹, and topological phase transitions in Floquet quasi-crystals³¹. Of all synthetic-dimension lattices, one promising platform is the temporal mesh lattice which can be constructed by mapping conceptually from two coupled fiber loops²²⁻³¹. Thanks to the convenient and flexible introduction of modulations within the fiber loops, effective gauge fields can be readily created in the lattices, which give rise to

various intriguing light transport phenomena, such as Bloch oscillations²², Berry-curvature induced anomalous transport²⁶, Anderson localization^{25,30}, topological phase transitions and Hofstadter butterfly³¹. However, it remains fully unclear whether such discrete-time photonic quantum walks can realize the Dunlap-Kenkre model of DL, thus providing a fertile setting to demonstrate high-order DL regimes that have been so far elusive.

In this work, we show that discrete-time photonic quantum walks in synthetic temporal mesh lattices can indeed realize the continuous Dunlap-Kenkre model of DL, and report on the observations of high-order DL under artificial ac electric fields of strong amplitude. The ac electric field originates from a harmonic oscillating vector potential created by introducing opposite phase modulations within the two fiber loops. We show that the width of lattice's quasi-energy band structure is modified by the ac electric field, which collapses as the field's amplitude is tuned to a series of Bessel function's roots, corresponding to various orders of DLs. In the experiments, we observe up to fifth-order DL and demonstrate that higher-order DLs possess smaller mean-square displacements during propagation and stronger robustness against stochastic noises than lower-order ones. Furthermore, by combining the less-localized first-order and highly-localized fifth-order DLs, we propose a temporal cloaking scheme where the first- and fifth-order DLs contribute to the opening and closing of the temporal cloak. It shows that both the cloak's width and opening time can be freely tuned to fit the protection requirements of temporal events. The study on higher-order DLs and tunable temporal cloaking may find great applications in robust signal transmission, processing, and temporal waveform reshaping.

Results

Theoretical model of high-order DLs. A synthetic temporal lattice can be created by connecting two coupled fiber loops with a tiny length difference, as illustrated in the inset of Fig. 1a. The length difference can induce a relative time delay for pulse traveling in the two loops, forming a pulse train that can be mapped to a discretized temporal lattice²²⁻³¹. The lattice site n labels the transverse pulse position while the step m represents the pulse circulation number in the two loops. After each circulation, the pulse in the long loop obtains a time delay, corresponding to the hopping from n to $n+1$. While in the short loop it obtains a time advance, resulting in the hopping from n to $n-1$ sites.

To create an additional ac electric field within the temporal lattice, we can apply opposite phase modulations of $\pm\phi(m)$ in the two fiber loops. Here we consider the simplest case of sinusoidally varying phase modulation $\phi(m) = \Delta\phi\cos(\omega m + \varphi)$, where $\Delta\phi$, ω and φ represent the modulation amplitude, frequency and initial phase, respectively. Then a pulse will acquire a phase shift of $-\phi(m)$ from site n to $n-1$ and an opposite phase of $\phi(m)$ when travelling from n to $n+1$. Such a direction-dependent phase factor is a photonic analogue of Peierls phase, which corresponds to an effective vector potential $A_{eff} = \phi(m)$ applied in the temporal lattice^{33,41,42}. Note that the vector potential itself is harmonically oscillating in time, it can lead to an ac electric field for photons³², i.e., $E_{eff}(m) = -dA_{eff}/dm = \omega\Delta\phi\sin(\omega m + \varphi)$.

Under the action of the ac electric field, the pulse evolution in the temporal lattice can be described by the following equation

$$\begin{cases} u_n^m = [\cos(\beta)u_{n+1}^{m-1} + i\sin(\beta)v_{n+1}^{m-1}]e^{-i\phi(m)} \\ v_n^m = [i\sin(\beta)u_{n-1}^{m-1} + \cos(\beta)v_{n-1}^{m-1}]e^{i\phi(m)} \end{cases}, \quad (1)$$

where u_n^m and v_n^m denote the pulse amplitudes in short and long loops at lattice site n and time step m . The power splitting ratio of the directional coupler is defined as $\sin^2(\beta)/\cos^2(\beta)$, with $\beta \in [0, \pi/2]$. Consider the eigen Bloch mode supported by the temporal lattice

$$|\psi\rangle = \begin{pmatrix} u_n^m \\ v_n^m \end{pmatrix} = \begin{pmatrix} U \\ V \end{pmatrix} e^{iQn} e^{i\theta m}, \quad (2)$$

where $(U, V)^T$ denotes the eigenvector, Q and θ are the transverse Bloch momentum and longitudinal propagation constant, respectively. Substituting Eq. (2) into Eq. (1), we can obtain the instantaneous band structure of the temporal lattice (see Supplementary Note 1)

$$\theta_{\pm}[Q(m)] = \mp\cos(\beta)\cos[Q(m)] \pm \frac{\pi}{2}, \quad (3)$$

where $Q(m) = Q - \phi(m)$ is the time-dependent Bloch momentum, “ \pm ” denote the upper and lower branches of band structure. As shown in the band structure of Fig. 1b, the application of an ac electric field can induce the periodic shifting of Bloch momentum within a region of range $2\Delta\phi$ in the Brillouin zone. To get the averaging effect, we assume a slow modulation frequency $\omega = 2\pi/M$, where the integer M is the modulation period. In this limit, the time-independent quasi-energy band structure can be obtained by performing the time averaging of instantaneous band structure over one driving period, i.e., (see Supplementary Note 2)

$$\langle \theta_{\pm} \rangle = \frac{1}{M} \int_0^M \theta_{\pm}(m) dm = \mp J_0(\Delta\phi) \cos(\beta) \cos(Q) \pm \frac{\pi}{2}. \quad (4)$$

where $J_0(\Delta\phi)$ is the zeroth-order Bessel function. Figure 1c shows the quasi-energy band structure versus different modulation amplitude $\Delta\phi$ and its projection onto the $\langle \theta \rangle$ - $\Delta\phi$ plane. It shows that the effect of the ac electric field is to modify the bandwidth, i.e., the slope of quasi-energy band structure. Specifically, the bandwidth will collapse as $\Delta\phi$ is tuned to a series of zeros of J_0 function (labelled by the red lines and dots), at which different orders of DLs occur. The exact mapping of the discrete-time photonic quantum walk with the continuous Dunlap-Kenkre model of DL, obtained for a coupling ratio β close to $\pi/2$ and a slow modulation frequency, is presented in Supplementary Note 2. To see how the ac electric field controls the lattice evolution dynamics, we consider a Bloch-mode wave packet impinging on the lattice with initial Bloch momentum Q , the averaged group velocity can be derived from the quasi-energy band structure, which reads

$$\langle v_{g,\pm} \rangle = -\partial \langle \theta_{\pm} \rangle / \partial Q = \mp J_0(\Delta\phi) \cos(\beta) \sin(Q). \quad (5)$$

After a driving period M , the wave packet can accumulate a total transverse displacement

$$\Delta n_{\pm} = M \langle v_{g,\pm} \rangle = \mp M J_0(\Delta\phi) \cos(\beta) \sin(Q). \quad (6)$$

Meanwhile, the packet will experience the envelope broadening during propagation, which can be quantitatively described by the averaged diffraction coefficient

$$\langle D_{\pm} \rangle = \partial^2 \langle \theta_{\pm} \rangle / \partial^2 Q = \mp J_0(\Delta\phi) \cos(\beta) \cos(Q). \quad (7)$$

As $\Delta\phi$ takes one of the roots of J_0 function, both the wave packet transverse shifting and broadening vanish, $\langle v_{g,\pm} \rangle = \langle D_{\pm} \rangle = 0$, the packet will restore to its initial incident position with initial profile after each driving period, showing the characteristic features of periodic revival for DLs. However, since different orders of DLs share the common features of periodic wave-motion and broadening cancelation, one cannot distinguish them in terms of $\langle v_{g,\pm} \rangle$ and $\langle D_{\pm} \rangle$.

To distinguish different orders of DLs, one needs to inspect the explicit evolution process within a driving period. In fact, due to the non-vanishing instantaneous group velocity $v_{g,\pm}(m) = -\partial \theta_{\pm}(m) / \partial Q = \mp \cos(\beta) \sin[Q - \Delta\phi \cos(\omega m + \varphi)]$ and diffraction coefficient $D_{\pm}(m) = \partial^2 \theta_{\pm}(m) / \partial^2 Q = \mp \cos(\beta) \cos[Q - \Delta\phi \cos(\omega m + \varphi)]$, the wave packet experiences delocalization at each step within a driving period. Quantitatively, the degree of delocalization during propagation can be characterized by a statistic parameter of instantaneous mean-square displacement, $\langle n^2(m) \rangle$ ^{5,11,30}

$$\langle n^2(m) \rangle = \frac{\sum_n \left[n^2 \left(|u_n^m|^2 + |v_n^m|^2 \right) \right]}{\sum_n \left(|u_n^m|^2 + |v_n^m|^2 \right)}. \quad (8)$$

which measures the displacement of wave-packet with respect to the initial reference position. According to Eq. (8), $\langle n^2(m) \rangle$ depends quadratically on the occupied position n , indicating that it will increase with the packet's transverse displacement and diffraction spreading. Different-order DLs exhibit different wave-packet dynamics and hence $\langle n^2(m) \rangle$ evolutions. More specifically, the maximum mean-square displacement $\langle n^2(m) \rangle_{\max}$ within a single driving period can be adopted to characterize the localization strength of different-order DLs.

Experimental realization of high-order DLs. To verify the theoretical analysis, we experimentally build a coupled double fiber-loops circuit, as shown schematically in Fig. 2. Two fiber loops with an average length of ~ 5 km are connected via a 75:25 (corresponding to $\beta = \pi/3$) directional coupler. The length difference of the two loops is ~ 30 m, corresponding to a relative time delay of ~ 150 ns. The required sinusoidal phase modulation is provided by the incorporated phase modulator (PM) in the short loop driven by an arbitrary waveform generator (AWG). The initial Bloch-mode wave packet is prepared from a single optical pulse with duration time of ~ 100 ns injected from the long fiber loop (see Materials and Methods). The detection of wave packet evolution at each step is realized by recording the pulse-train intensity distributions extracted from the two loops. Other details about the experimental setup and measurement are also provided in Materials and Methods.

In the experiment, we excite a Bloch-mode wave packet from the upper band as the incidence, which carries an initial Bloch momentum $Q = \pi/2$. Figure 3a depicts the packet transverse displacement Δn after a single driving period as a function of the phase modulation amplitude $\Delta\phi$. Here the modulation frequency is fixed as $\omega = \pi/60$, corresponding to a driving period of $M = 2\pi/\omega = 120$. It shows that the displacement Δn follows an oscillatory variation of J_0 Bessel function with the increase of $\Delta\phi$, which is in perfect accordance with theoretical prediction of Eq. (6). Specifically, $\Delta n = 0$ occurs at $\Delta\phi = 2.4, 5.5, 8.7, 11.8$ and 14.9 , as denoted by the blue dots, clearly validating DLs from the first to fifth orders.

In Figs. 3b and 3c, we illustrate the simulated and experimental wave packet evolutions by choosing several specific modulation amplitudes of $\Delta\phi = 0, 3.8, 2.4, 14.9$. For comparison, we firstly

consider the packet evolution in the absence of modulation with $\Delta\phi = 0$. In this case, the packet exhibits a constant group velocity of $v_g = -\cos(\beta)\sin(Q) = -0.5$, corresponding to a maximum left displacement of $\Delta n = v_g M = -60$, as shown in Fig. 3b(i). In Fig. 3c(i), we get a measured displacement of $\Delta n = -59.2$, which matches well with the theoretical prediction. For a non-zero modulation amplitude $\Delta\phi = 3.8$, as shown in Figs. 3b(ii) and 3c(ii), the packet exhibits a maximum right displacement of $\Delta n = 24.5$, in accordance with theoretical result of $\Delta n = -J_0(\Delta\phi)\cos(\beta)\sin(Q) = 24.2$. It shows that the presence of modulation (ac electric field) can modify the wave-packet group velocity, which reaches the maximum displacement for the field-free case. Additionally, the wave packet manifests a curved evolution trajectory under the ac field driven with a time-varying group velocity, in contrast to the straight trajectory with a constant velocity for the field-free case. Also note that both the field-driven and field-free cases exhibit diffraction-free evolutions without packet broadening. This is attributed to the vanishing diffraction coefficient $\langle D \rangle = 0$ for $Q = \pi/2$ according to Eq. (7).

We show the simulated and measured pulse intensity evolutions for the 1st- and 5th-order DLs in Figs. 3b(iii), 3b(iv), 3c(iii) and 3c(iv). One sees that the wave packet displays an oscillatory trajectory during propagation and restores to its initial position and profile after a single driving period. The packet for the 1st-order DL possesses much larger oscillation amplitude compared to that of the 5th-order one. Additionally, the wave packet experiences obvious diffraction spreading during the 1st-order DL process. In contrast, the packet width remains nearly unchanged with negligible broadening for the 5th-order DL. Hence, higher-order DLs possess much stronger localization strength than the lower-order ones.

To quantitatively characterize the localization strength of different orders of DLs, we plot in Fig. 3d the measured mean-square displacement $\langle n^2(m) \rangle$ evolutions by choosing the 1st- and 5th-order cases. The comprehensive comparisons of pulse intensity evolutions and mean-square displacements from the 1st- to 5th-order DLs are provided in Supplementary Note 3. Here, at each step m , the mean-square displacement $\langle n^2(m) \rangle$ for the 5th-order DL is much smaller than that of the 1st-order one. As also summarized in the inset of Fig. 3d, the maximum mean-square displacement $\langle n^2(m) \rangle_{\max}$ decreases from 48.1 to 14.9 as the order increases from 1 to 5, clearly demonstrating that the wave packet can be better localized for the higher-order DL. The mechanism for enhanced localization strength of high-order DL can be attributed to the faster variation rate of wave-packet momentum

under larger ac electric field driving (see Supplementary Note 4). As shown schematically in Supplementary Fig. S3, a larger electric field can drive a Bloch wave packet to oscillate across a larger regime in the extended Brillouin zone, leading to more times of packet Bragg reflections at each Brillouin zone edge and center. More frequent Bragg reflections will cancel the net accumulated packet motion in one direction within a driving period and hence give rise to the stronger localization strength.

Enhanced robustness against random noises of high-order DLs. In this section, we investigate the robustness of different orders DLs against external random noises. Without loss of generality, we consider a randomly time-varying modulation phase superimposed onto the sinusoidally varying modulation phase, i.e., $\phi(m) = \Delta\phi\cos(\omega m + \varphi) + \delta\phi\text{rand}(m)$, where $\text{rand}(m)$ denotes the random function with a uniform probability from -0.5 to 0.5 , $\delta\phi$ represents the strength of fluctuation. The superimposed modulation waveforms are schematically shown in Fig. 4a, where we have chosen a strong and a weak ac field, respectively. In the presence of the random noise, DLs of different orders will degrade, giving rise to the broadening of wave packet. Quantitatively, to describe the degree of wave-packet broadening, we utilize the inverse participation ratio (*IPR*), which is defined as^{25,29}

$$IPR = \frac{\sum_n \left(|u_n^m|^2 + |v_n^m|^2 \right)^2}{\left[\sum_n \left(|u_n^m|^2 + |v_n^m|^2 \right) \right]^2}, \quad (9)$$

with $0 < IPR \leq 1$. A higher *IPR* reflects less wave packet spreading and thus better localization, also suggesting stronger robustness against external noise.

The solid curve in Fig. 4b depicts the theoretical variation of *IPR* after one driving period as the modulation amplitude increase continuously from $\Delta\phi = 0$ to $\Delta\phi = 15$. Here we have kept the random noise strength unchanged with $\delta\phi = 0.15\pi$. It shows that the *IPR* reaches a peak value at each order of DLs, indicating that DL can efficiently suppress the noise-induced wave packet broadening. To verify this, in experiment we choose modulation amplitudes at different orders of DLs, where the measured *IPR* can match well with the theoretical results. Moreover, as the order increases from 1 to 5, the *IPR* for different order DLs increases from 0.06 to 0.13, suggesting that higher-order DLs possess superior robustness against stochastic noises over lower-order ones. Figures 4c-4e illustrate the measured pulse intensity evolutions for $\Delta\phi = 0$, 2.4 (1st-order DL) and 14.9 (5th-order DL),

respectively. Here for each case, we have performed statistic averaging for 10 times of experiment results. Without the ac electric field, the wave packet experiences the most serious expansion, showing cone-like (ballistic) packet boundaries (Fig. 4c). For the 1st-order DL, the wave packet width has expanded by about 5 times after one driving period (Fig. 4d). In contrast, the wave-packet width almost conserves for the 5th-order DL thanks to the stronger robustness against noise (Fig. 4e). More detailed pulse intensity evolutions from the 1st- to 5th-order DLs in the presence of the random noises are shown in Supplementary Note 5. The enhanced robustness of high-order DLs against noises can be explained from the slope of quasi-energy band structures at each zero of J_0 Bessel function. As shown in Fig. 1c, the slope of J_0 Bessel function at each zero becomes smaller as the zero's order increases, such that under the same perturbation strength $\delta\phi$, higher-order DL at higher-order zero gets smaller bandwidth expansion from the collapsed point and hence stronger localization properties.

Tunable temporal cloaking by combining higher- and lower-order DLs. As we demonstrate in previous sections, higher-order DL manifests smaller packet displacement and stronger robustness against noises, which are desirable for robust signal transmission. On the other hand, lower-order DL exhibits larger displacement within a driving period and can restore to its initial position after the driving period, which are helpful for signal delay and reconstruction. In this section, we combine both higher- and lower-order DLs to design a temporal cloaking scheme. As shown schematically in Fig. 5a, a wave packet impinges into the first region where we use fifth-order DL to realize robust signal transmission. At the interface of region 1 and 2, we use first-order DL and introduce a constant relative phase shift to achieve wave-packet splitting. Such a splitting can circumvent an event, thus forming a temporal cloak. Then we switch back to high-order DL at the interface of regions 2 and 3, where packet recombination occurs after finishing one driving period.

The relative constant phase shift between region 2 and 1 plays a role of an effective gauge potential, which can induce a constant band shifting and hence wave packet splitting. Assume that the constant biased phase in region 1 and 2 is denoted by ϕ_l , ($l=1, 2$), such that the band structures are $\theta_{l,\pm} = \mp \cos(\beta) \cos(Q - \phi_l) \pm \pi/2$ (Fig. 5b), with the corresponding eigen states given by

$$|\psi_{l,\pm}\rangle = \begin{pmatrix} U_{l,\pm} \\ V_{l,\pm} \end{pmatrix} e^{iQn} e^{i\theta_{l,\pm}m}, \quad (10)$$

where

$$\begin{pmatrix} U_{l,\pm} \\ V_{l,\pm} \end{pmatrix} = \frac{1}{\sqrt{1+e^{\mp 2\lambda_l}}} \begin{pmatrix} 1 \\ -e^{\mp \lambda_l} \cdot e^{-i(Q-\phi_l)} \end{pmatrix}, \quad (11)$$

and $\lambda_l = \text{arcsinh}[\cot(\beta)\sin(Q-\phi_l)]$. Consider a wave packet incidence from the upper band in region 1, it will exhibit refraction at the interface of region 1 and 2. According to the conservation law of Bloch momentum at the interface, as denoted by the dashed line in Fig. 5b, the incident wave packet in region 1 can match two packets of the two branches in region 2, i.e.,

$$\begin{pmatrix} U_{1,+} \\ V_{1,+} \end{pmatrix} = c_{2,+} \begin{pmatrix} U_{2,+} \\ V_{2,+} \end{pmatrix} + c_{2,-} \begin{pmatrix} U_{2,-} \\ V_{2,-} \end{pmatrix}, \quad (12)$$

where $c_{2,+}$ and $c_{2,-}$ are the occupation coefficients of the upper and lower bands. By combing Eqs. (11) and (12), we further obtain

$$\begin{cases} c_{2,+} = (V_{1,+}U_{2,-} - U_{1,+}V_{2,-}) / (U_{2,-}V_{2,+} - U_{2,+}V_{2,-}) \\ c_{2,-} = (U_{1,+}V_{2,+} - V_{1,+}U_{2,+}) / (U_{2,-}V_{2,+} - U_{2,+}V_{2,-}) \end{cases}. \quad (13)$$

Specifically, for $\phi_2 - \phi_1 = \pi/2$, we can achieve $|c_{2,+}|^2 = |c_{2,-}|^2 = 0.5$, indicating the packet is equally splitting in power. In region 2, the two split wave packets exhibit 1st-order DLs under a low-amplitude ac electric field driving. Since the two packets occupying two bands have opposite group velocities, they will transport separately with mirror-symmetric trajectories, therefore creating a time window, i.e., a temporal cloak. After finishing one-period DL in region 2, the two packets restore to their initial positions and manifest a packet recombination at the interface of region 2 and 3, leading to the closing of the temporal cloak. Note that due to the periodic revival nature of DL, the packet recombination process is just the time reversal of the packet splitting. In region 3, the packet then goes on exhibiting fifth-order DL.

In our experiments, the temporal event to be cloaked is mimicked by the pulse intensity absorption between $n = -1$ and $n = 1$ at $m = 80$ step realized by changing the intensity modulators' transmittances of two loops. For comparison, we firstly show the wave packet evolution of the 5th-order DL without temporal cloak in Fig. 5c. It shows that even though the 5th-order DL manifests strong robustness against the noise in the driving electric field, it is still severely affected by the absorption event. In contrast, by introducing the above temporal cloak, as depicted in Fig. 5d,

the absorption event can be circumvented perfectly by the time window, such that the packet restores to its input state of the 5th-order DL after the cloaking region. Figure 5e illustrates the output wave packet intensity distributions detected at step $m = 162$ with and without the temporal cloak. By comparing with the packet direct transmission without absorption event, the output packet is completely unaffected with the protection of the temporal cloak, as if the event does not exist.

Finally, we demonstrate that the temporal cloak possesses flexible tunability both in the cloaking window size and its opening time. As shown in Fig. 6a, since the two split wave packets belonging to the lower and upper bands have positive and negative group velocities, they will propagate towards opposite directions. The width of the cloaking window is defined by the maximum spacing of the two split packets, which is reached at the center of one driving period $m = M/2$, i.e.,

$$W_{\max} = \int_0^{M/2} |v_{g,-}(m) - v_{g,+}(m)| dm = MW_0, \quad (14)$$

where $W_0 = 2\cos(\beta)\int_0^{1/2} \sin[\Delta\phi\sin(2\pi m/M)]d(m/M)$, denoting the averaging width increase within one step (see Supplementary Note 6). Equation (14) suggests that the cloaking window width is proportional to the driving period M , as also plotted in Fig. 6b. For experimental demonstrations, we design two cloaks of different sizes by choosing two driving periods of $M = 80$ and $M = 50$, respectively. Figure 6c shows the packet evolution with the two cloaks. The width of the first cloak reaches $W_{\max} = 31$ with $W_0 = 0.37$, such that it can circumvent three absorption events. While the size of the second cloak is smaller with the width being $W_{\max} = 17.5$, within which only one absorption event is cloaked. With its flexible tunability, our temporal cloak can adapt to random perturbation events with different triggering and duration time. Our paradigm may find potential applications in the scenarios of robust optical communications and signal processing.

Furthermore, our temporal cloaking scheme is quite different from the previously dispersion-based ones where the normal and anomalous group velocity dispersions (GVDs) of optical pulses contribute to the opening and closing of temporal cloak^{43,44}. Nevertheless, the GVD coefficient of optical fiber is usually hard to modify, not to mention dynamic modification of GVD coefficient, which highly limits the manipulation of the cloaking window size and opening time. Here, by creating artificial ac electric field and combing lower- and higher-order DLs, we have demonstrated a temporal cloak with dynamically controllable cloaking size and opening time, which

enables the cloaking of random temporal events and thus improves the quality of signal transmission^{45,46}.

Discussion

In conclusion, we have shown that photonic quantum walks in synthetic temporal mesh lattices can provide a fertile platform to realize the Dunlap-Kenkre model of DL, and experimentally demonstrated different orders of DLs by artificial ac electric fields from sinusoidal phase modulations. By tuning the modulation amplitude to the roots of 0th-order Bessel function, we have realized the collapse of quasi-energy band structures and observed from first- up to fifth-order DLs, with a corresponding increase of the degree of localization over the full oscillation cycle. Remarkably, in the presence of external random noise, the higher-order DLs display much greater robustness against noise. The strategic quasi-energy band engineering enabled by our photonic platform can be harnessed to realize temporal cloaking. Specifically, we designed and experimentally demonstrated a temporal cloaking scheme by combining the higher and lower-order DLs, with excellent tunability in terms of both cloaking window size and its opening time. As a final comment, it should be noted that the order of DLs is not unlimited due to onset of Landau-Zener tunneling under sufficiently large electric-field driving, corresponding to inevitable band mixing and hence wave-packet energy oscillations for DLs^{3,4,40}. Furthermore, it should be mentioned that the tunability size of the temporal cloak is also not unlimited due to the presence of inevitable noise from the optical amplifier within the fiber loops. The tunability could be further optimized by using lower-power amplifier with relatively lower noises, for which other lower-loss optical components should also be utilized.

Our work has established a versatile testbed of synthetic temporal lattices for studying ac-driven photon Hermitian dynamics, which could inspire further theoretical and experimental studies as well as unravel new phenomena beyond the traditional Hermitian paradigm of discretized light transport. Thanks to the ability to engineer gain and loss in the synthetic mesh lattice setups^{23,31}, the correspondence between photonic quantum walks and the Dunlap-Kenkre model, unravelled in this work, could also pave the way toward the experimental demonstration of DL effects and related phenomena in the non-Hermitian realm. These include the experimental access to dynamical

localization in parity-time systems⁴⁷ and the observation non-Bloch band collapse and chiral tunneling in lattices displaying the non-Hermitian skin effect^{29,48}. From the perspective of applications, due to the excellent tunability and strong robustness against noises, the high-order DLs we achieved could hold great promise for robust signal transmission, protection, storage and processing.

Methods

Experimental setup and measurement. The light pulses are generated by modulating a continuous-wave (cw) light beam with an intensity modulator (IM), which is driven by the pulse from an arbitrary waveform generator (AWG). After injected into the long loop, the pulse will circulate in the two loops. During circulation, the optical loss is compensated by erbium-doped fiber amplifiers (EDFAs). To overcome the transient of EDFA, the signal pulse is combined with a pilot light operated at a wavelength of 1530 nm. Then, the pilot light and spontaneous emission noise are removed by band-pass filters (BPFs). To detect the optical pulses, we couple the signals out of the loops and record them by photodiodes (PDs) and oscilloscopes (OSCs). The polarization states of light pulses is controlled through polarization controllers (PCs). Polarization beam splitter (PBS) and the subsequent PD are utilized to monitor the polarization state. The phase modulation is only imposed in the short loop, which has a form of $-2\phi(m)$. The difference between the modulation phases in the two loops is $-2\phi(m)$, which is same with the one mentioned in the main text. Since not the phase but the phase difference has physical meaning, such scheme of phase modulation is equivalent to the one mentioned in the main text. Finally, after 160 circulations in the loops, all pulses are absorbed by switching off IMs. In addition, all the modulators are driven by AWGs.

Preparation of Gaussian-envelope wave packet. To generate a Gaussian-envelope pulse sequence with specific Bloch momentum, we inject a single optical pulse into the long loop and impose phase and intensity modulations into the two loops^{24,26}. By controlling the driving signals of IMs, the short loop is switched on and off alternately with the increase of the circulation number m while the long loop stays on during the circulation. After 30 circulations, a pulse train with Gaussian envelope is formed. Moreover, by imposing a constant phase shift α in the short loop during the 30 circulations,

the Bloch momentum of wave packet can be chosen and has a form of $Q = (\pi - \alpha)/2$. To excite the eigen mode at the upper or lower band, we set phase and intensity modulations at the 31th circulation according to the eigen vector.

Data availability

The data that support the findings of this study are available from the corresponding authors upon reasonable request.

References

1. Bloch, F. Über die quantenmechanik der elektronen in kristallgittern. *Z. Phy.* **52**, 555-600 (1928).
2. Waschke, C. *et al.* Coherent submillimeter-wave emission from Bloch oscillations in a semiconductor superlattice. *Phys. Rev. Lett.* **70**, 3319-3322 (1993).
3. Zener, C. Non-adiabatic crossing of energy levels. *Proc. R. Soc. London A* **137**, 696-702 (1932).
4. Rosam, B. *et al.* Field-induced delocalization and Zener breakdown in semiconductor superlattices. *Phys. Rev. Lett.* **86**, 1307-1310 (2001).
5. Dunlap, D. H. & Kenkre, V. M. Dynamic localization of a charged particle moving under the influence of an electric field. *Phys. Rev. B* **34**, 3625-3633 (1986).
6. Holthaus, M. Collapse of minibands in far-infrared irradiated superlattices. *Phys. Rev. Lett.* **69**, 351-354 (1992).
7. Dignam, M. M. & de Sterke, C. M. Conditions for dynamic localization in generalized ac electric fields. *Phys. Rev. Lett.* **88**, 046806 (2002).
8. Anderson, P. W. Absence of diffusion in certain random lattices. *Phys. Rev.* **109**, 1492-1505 (1958).
9. Fishman, S., Grepel, D. R. & Prange, R. E. Chaos, quantum recurrences, and Anderson localization. *Phys. Rev. Lett.* **49**, 509-512 (1982).
10. Segev, M., Silberberg, Y. & Christodoulides, D. N. Anderson localization of light. *Nat. Photon.* **7**, 197-204 (2013).
11. Longhi, S. *et al.* Observation of dynamic localization in periodically curved waveguide arrays. *Phys. Rev. Lett.* **96**, 243901 (2006).
12. Szameit, A. *et al.* Polychromatic dynamic localization in curved photonic lattices. *Nat. Phys.* **5**, 271-275 (2009).
13. Szameit, A. *et al.* Observation of two-dimensional dynamic localization of light. *Phys. Rev. Lett.* **104**, 223903 (2010).
14. Xu, Y.-L. *et al.* Experimental realization of Bloch oscillations in a parity-time synthetic silicon photonic lattice. *Nat. Commun.* **7**, 11319 (2016).
15. Crespi, A., Corrielli, G., Valle, G. D., Osellame, R. & Longhi, S. Dynamic band collapse in photonic graphene. *New Journal of Physics* **15**, 013012 (2013).
16. Iyer, R., Aitchison, J. S., Wan, J., Dignam, M. M. & de Sterke, C. M. Exact dynamic localization in curved AlGaAs optical waveguide arrays. *Opt. Express* **15**, 3212-3223 (2007).
17. Szameit, A. *et al.* Image reconstruction in segmented femtosecond laser-written waveguide arrays, *Appl. Phys. Lett.* **93**, 181109 (2008).

18. Joushaghani, A. *et al.* Generalized exact dynamic localization in curved coupled optical waveguide arrays, *Phys. Rev. Lett.* **109**, 103901 (2012).
19. Fang, K., Yu, Z. & Fan, S. Realizing effective magnetic field for photons by controlling the phase of dynamic modulation. *Nat. Photon.* **6**, 782-787 (2012).
20. Yuan, L. & Fan, S. Three-dimensional dynamic localization of light from a time-dependent effective gauge field for photons. *Phys. Rev. Lett.* **114**, 243901 (2015).
21. Bersch, C., Onishchukov, G. & Peschel, U. Spectral and temporal Bloch oscillations in optical fibres. *Appl. Phys. B* **104**, 495 (2011).
22. Regensburger, A. *et al.* Photon propagation in a discrete fiber network: An interplay of coherence and losses. *Phys. Rev. Lett.* **107**, 233902 (2011).
23. Regensburger, A. *et al.* Parity-time synthetic photonic lattices. *Nature* **488**, 167-171 (2012).
24. Wimmer, M. *et al.* Optical diametric drive acceleration through action-reaction symmetry breaking. *Nat. Phys.* **9**, 780-784 (2013).
25. Vatanik, I. D., Tikan, A., Onishchukov, G., Churkin, D. V. & Sukhorukov, A. A. Anderson localization in synthetic photonic lattices. *Sci. Rep.* **7**, 4301 (2017).
26. Wimmer, M., Price, H. M., Carusotto, I. & Peschel, U. Experimental measurement of the Berry curvature from anomalous transport. *Nat. Phys.* **13**, 545-550 (2017).
27. Wang, S., Qin, C., Wang, B. & Lu, P. Discrete temporal talbot effect in synthetic mesh lattices. *Opt. Express* **26**, 19235-19246 (2018).
28. Wang, S., Wang, B. & Lu, P. Pt-symmetric talbot effect in a temporal mesh lattice. *Phys. Rev. A* **98**, 043832 (2018).
29. Weidemann, S. *et al.* Topological funneling of light. *Science* **368**, 311-314 (2020).
30. Weidemann, S., Kremer, M., Longhi, S. & Szameit, A. Coexistence of dynamical delocalization and spectral localization through stochastic dissipation. *Nat. Photon.* **15**, 576-581 (2021).
31. Weidemann, S., Kremer, M., Longhi, S. & Szameit, A. Topological triple phase transition in non-hermitian floquet quasicrystals. *Nature* **601**, 354-359 (2022).
32. Qin, C., Yuan, L., Wang, B., Fan, S. & Lu, P. Effective electric-field force for a photon in a synthetic frequency lattice created in a waveguide modulator. *Phys. Rev. A* **97**, 063838 (2018).
33. Qin, C. *et al.* Spectrum control through discrete frequency diffraction in the presence of photonic gauge potentials. *Phys. Rev. Lett.* **120**, 133901 (2018).
34. Dutt, A. *et al.* Experimental band structure spectroscopy along a synthetic dimension. *Nat. Commun.* **10**, 3122 (2019).
35. Wang, K., Dutt, A., Wojcik, C. C. & Fan, S. Topological complex-energy braiding of non-hermitian bands. *Nature* **598**, 59-64 (2021).

36. Wang, K. *et al.* Generating arbitrary topological windings of a non-hermitian band. *Science* **1**, 1240-1245 (2021).
37. Luo, X.-W. *et al.* Synthetic-lattice enabled all-optical devices based on orbital angular momentum of light. *Nat. Commun.* **8**, 16097 (2017).
38. Yuan, L., Lin, Q., Xiao, M. & Fan, S. Synthetic dimension in photonics. *Optica* **5**, 1396-1405 (2018).
39. Cardano, F. *et al.* Detection of zak phases and topological invariants in a chiral quantum walk of twisted photons. *Nat. Commun.* **8**, 15516 (2017).
40. D’Errico, A. *et al.* Bloch–Landau–Zener dynamics induced by a synthetic field in a photonic quantum walk. *APL Photon.* **6**, 020802 (2021).
41. Fang, K., Yu, Z. & Fan, S. Photonic aharonov-bohm effect based on dynamic modulation. *Phys. Rev. Lett.* **108**, 153901 (2012).
42. Lin, Q. & Fan, S. Light guiding by effective gauge field for photons. *Phys. Rev. X* **4**, 031031 (2014).
43. Fridman, M., Farsi, A., Okawachi, Y. & Gaeta, A. L. Demonstration of temporal cloaking. *Nature* **481**, 62-65 (2012).
44. Lukens, J. M., Leaird, D. E. & Weiner, A. M. A temporal cloak at telecommunication data rate. *Nature* **498**, 205-208 (2013).
45. Lukens, J. M., Metcalf, A. J., Leaird, D. E. & Weiner, A. M. Temporal cloaking for data suppression and retrieval. *Optica* **1**, 372-375 (2014).
46. Cortés, L. R., Seghilani, M., Maram, R. & Azaña, J. Full-field broadband invisibility through reversible wave frequency-spectrum control. *Optica* **5**, 779-786 (2018).
47. Longhi, S. Dynamic localization and transport in complex crystals. *Phys. Rev. B* **80**, 235102 (2009).
48. Longhi, S. Non-Bloch-band collapse and chiral Zener tunneling. *Phys. Rev. Lett.* **124**, 066602 (2020).

Acknowledgements

The work is supported by the National Natural Science Foundation of China (No. 11974124, No. 12021004, No. 12147151 and No. 61735006).

Author contributions

B.W. conceived the idea. S.W., C.Q. and F.Z. designed and performed the experiment. S.W., C.Q. and W.L. analysed the data. C.Q., B.W. and S.L. provided the theoretical support. B.W. and P.L. supervised the project. All authors contributed to the discussion of the results and writing of the manuscript.

Competing interests

The authors declare no competing interests.

Additional information

Supplementary information accompanies this paper at <https://doi.org/10.1038/xxxxx>.

Figures and captions

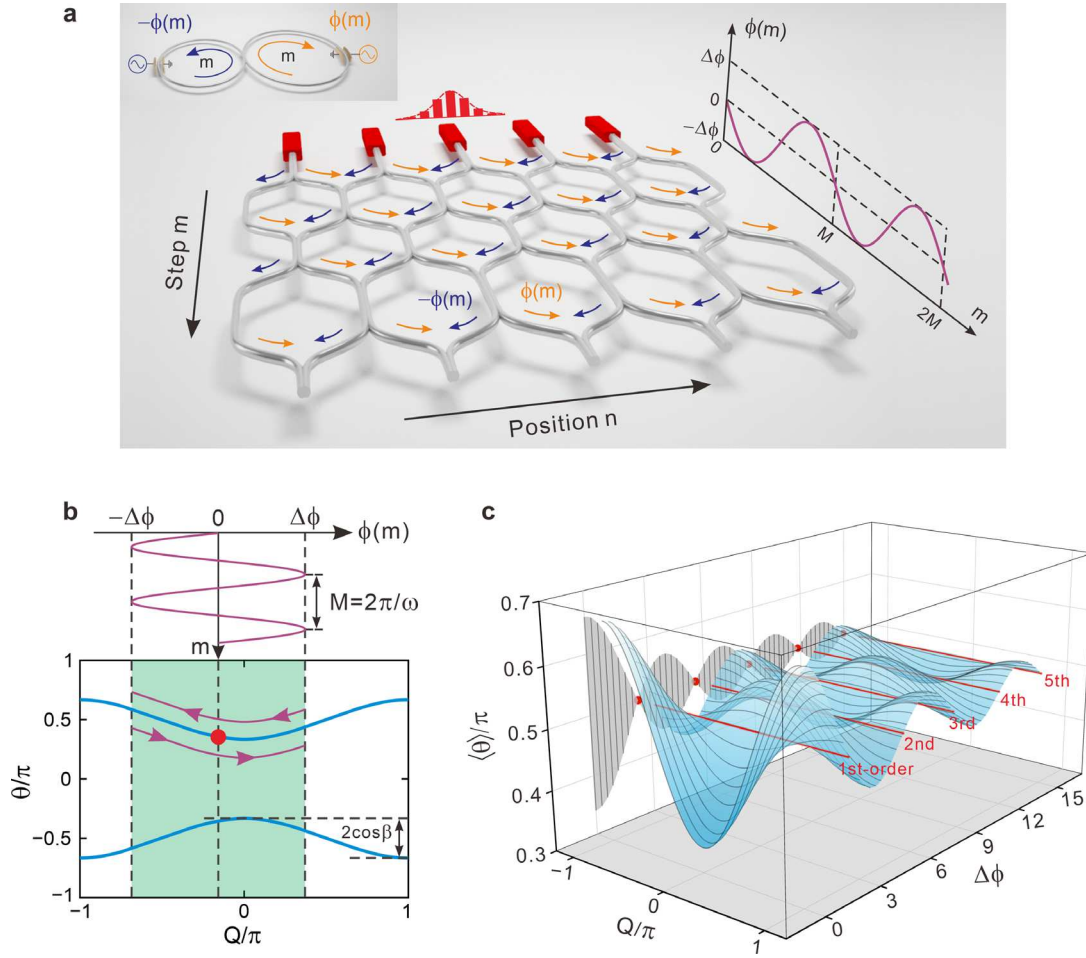


Fig. 1. Principle of different-order DLs in ac-driven synthetic temporal lattices. **a** Schematic diagram of a synthetic temporal mesh lattice constructed by mapping from two coupled fiber loops as shown by the inset figure. The opposite sinusoidal phase modulations $\pm\phi(m)$ are incorporated into the two fiber loops to generate a direction-dependent phase factor accompanying light hopping in the temporal lattice, corresponding to an effective time-periodic vector potential and hence an ac electric field therein. **b** Instantaneous band structure of the synthetic temporal lattice, where the Bloch momentum follows a periodic oscillation under the drive of the ac electric field with driving period $M = 2\pi/\omega$ and driving amplitude $\Delta\phi$. **c** Quasi-energy band structure versus the driving amplitude $\Delta\phi$ and its projection onto the $\langle\theta\rangle$ - $\Delta\phi$ plane, obtained by performing time averaging over the instantaneous band structure within one driving period M . Here only the upper band is plotted. The red lines denote the specific modulation amplitudes at J_0 function's zeros where the quasi-energy band structure collapses, corresponding to the occurrence of different-order DLs.

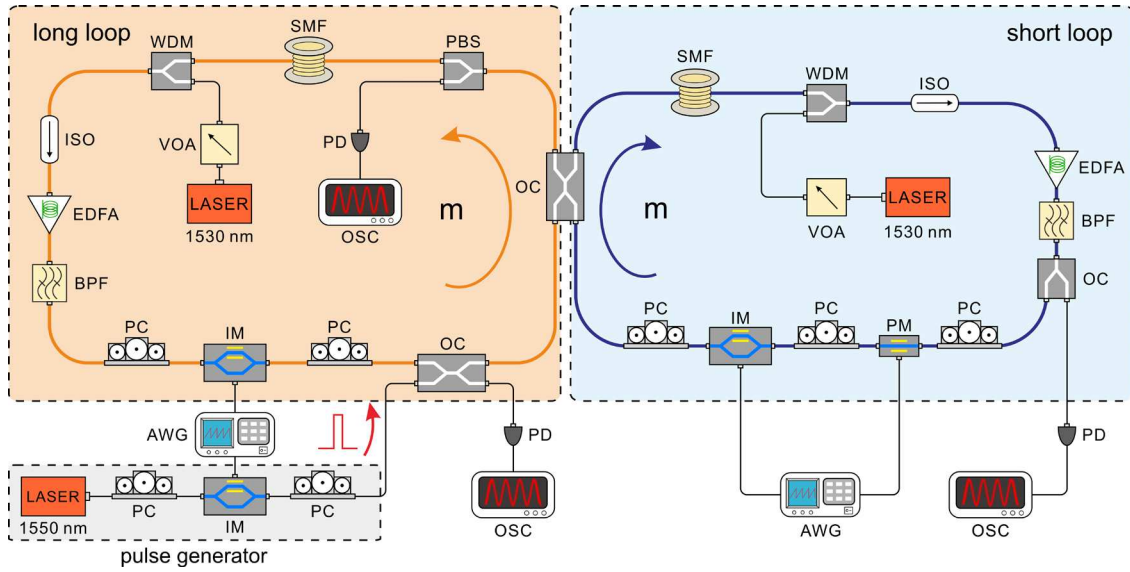


Fig. 2. Experimental setup. The yellow and blue loops denote the long and short loops and the yellow and blue arrows represent the pulse circulation directions within the two loops. All optical and electric components are as follows: Polarization controller (PC), intensity modulator (IM), optical coupler (OC), arbitrary waveform generator (AWG), single mode fiber (SMF), polarization beam splitter (PBS), photodiode (PD), oscilloscope (OSC), variable optical attenuator (VOA), isolator (ISO), wavelength division multiplexer (WDM), erbium-doped fiber amplifier (EDFA), band-pass filter (BPF), phase modulator (PM).

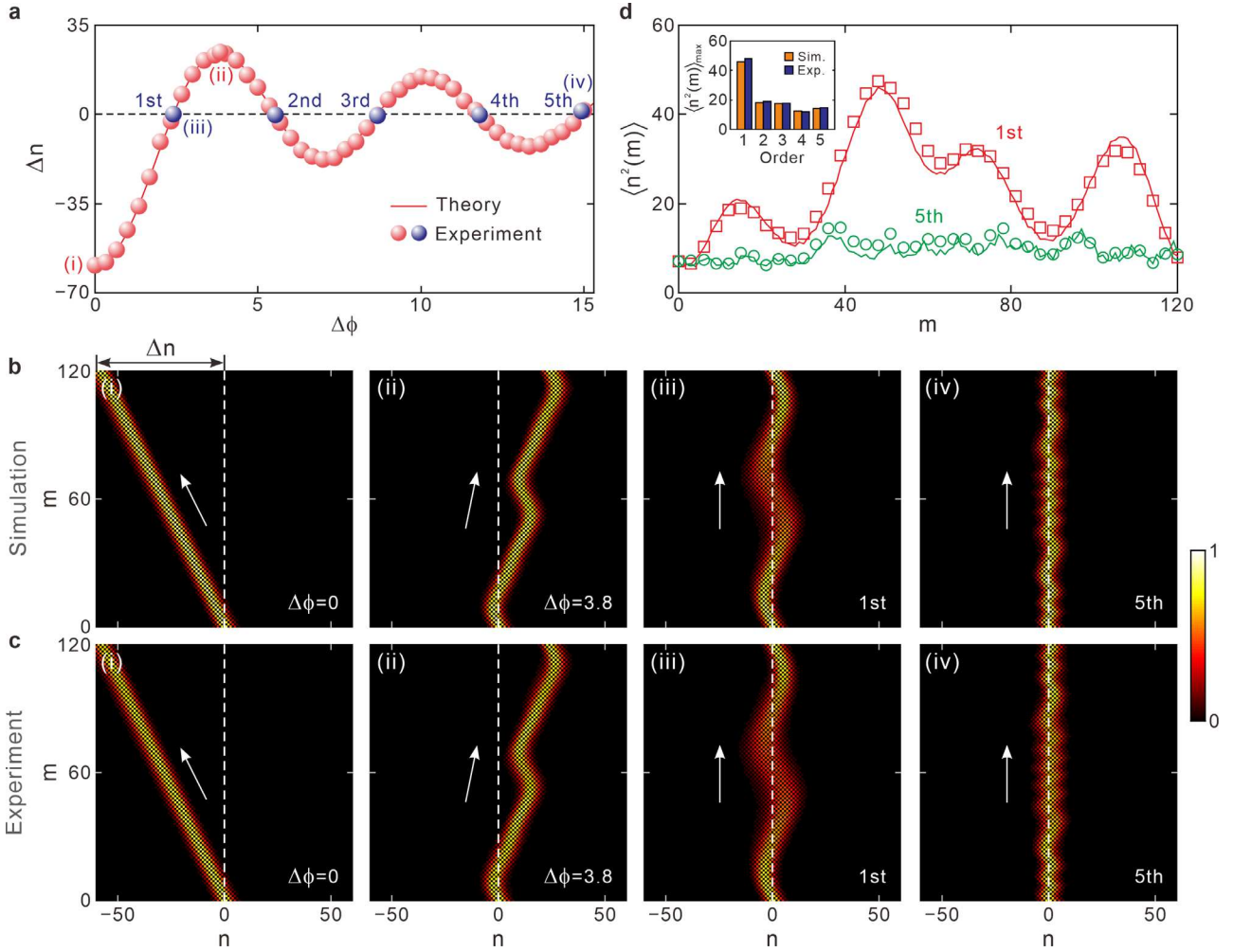


Fig. 3. Simulated and experimental results of different-order DLs. **a** Wave packet's transverse displacement Δn after a single driving period versus the phase modulation amplitude $\Delta\phi$. **b** Simulated pulse intensity evolution. (i) and (ii) correspond to directional transport with $\Delta\phi = 0$ and 3.8, respectively. (iii) and (iv) correspond to the 1st- and 5th-order DLs, respectively. **c** Measured pulse intensity evolution in one driving period with total step $M = 120$. **d** Mean-square displacement $\langle n^2(m) \rangle$ with respect to step m for 1st- and 5th-order DLs. The inset figure shows the maximum mean square displacement $\langle n^2(m) \rangle_{\max}$ versus the order of DL.

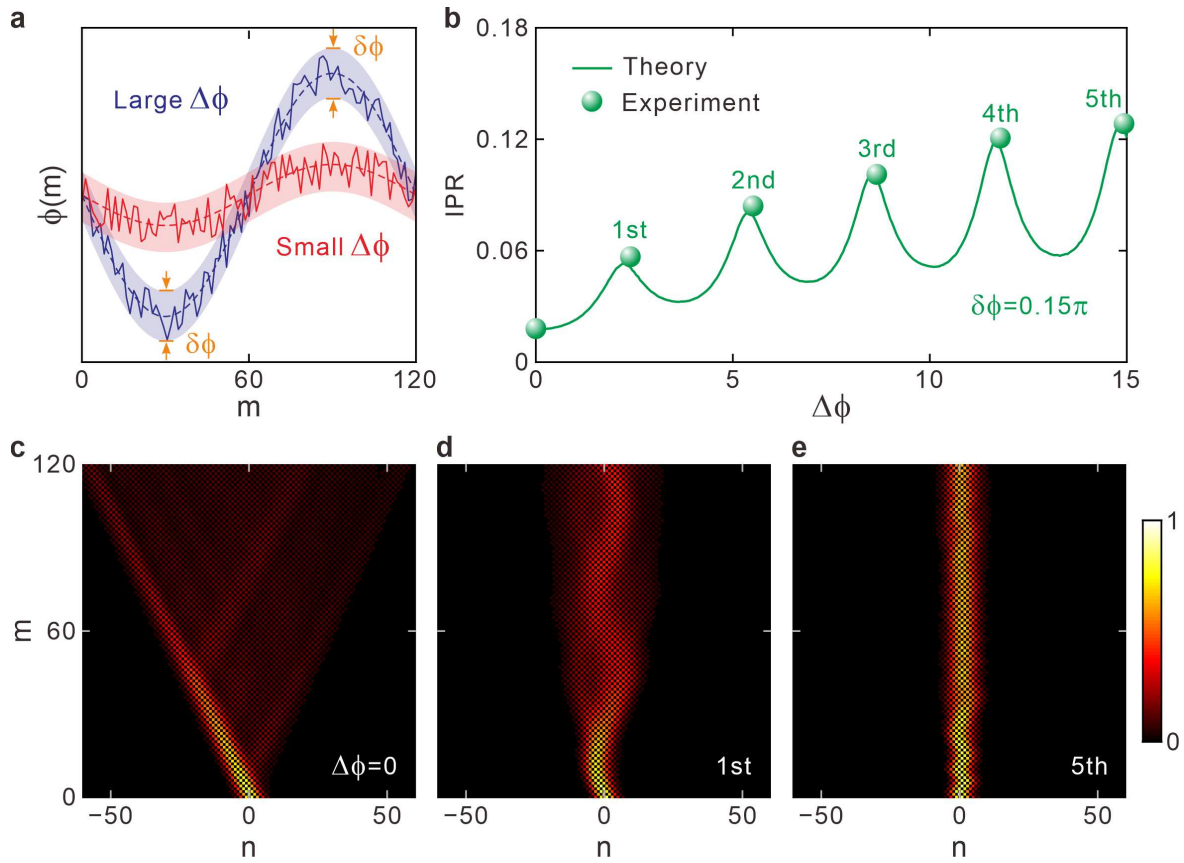


Fig. 4. Robustness comparison of different-order DLs against stochastic noises. **a** Sinusoidal phase modulation with a superimposed random noise. **b** Wave packet's inverse participation ratio IPR after one modulation cycle at step $m = 120$ in the presence of external random noise. **c** Measured pulse intensity evolutions for $\Delta\phi = 0$. **d**, **e** Measured pulse intensity evolutions for the 1st- and 5th-order DLs.

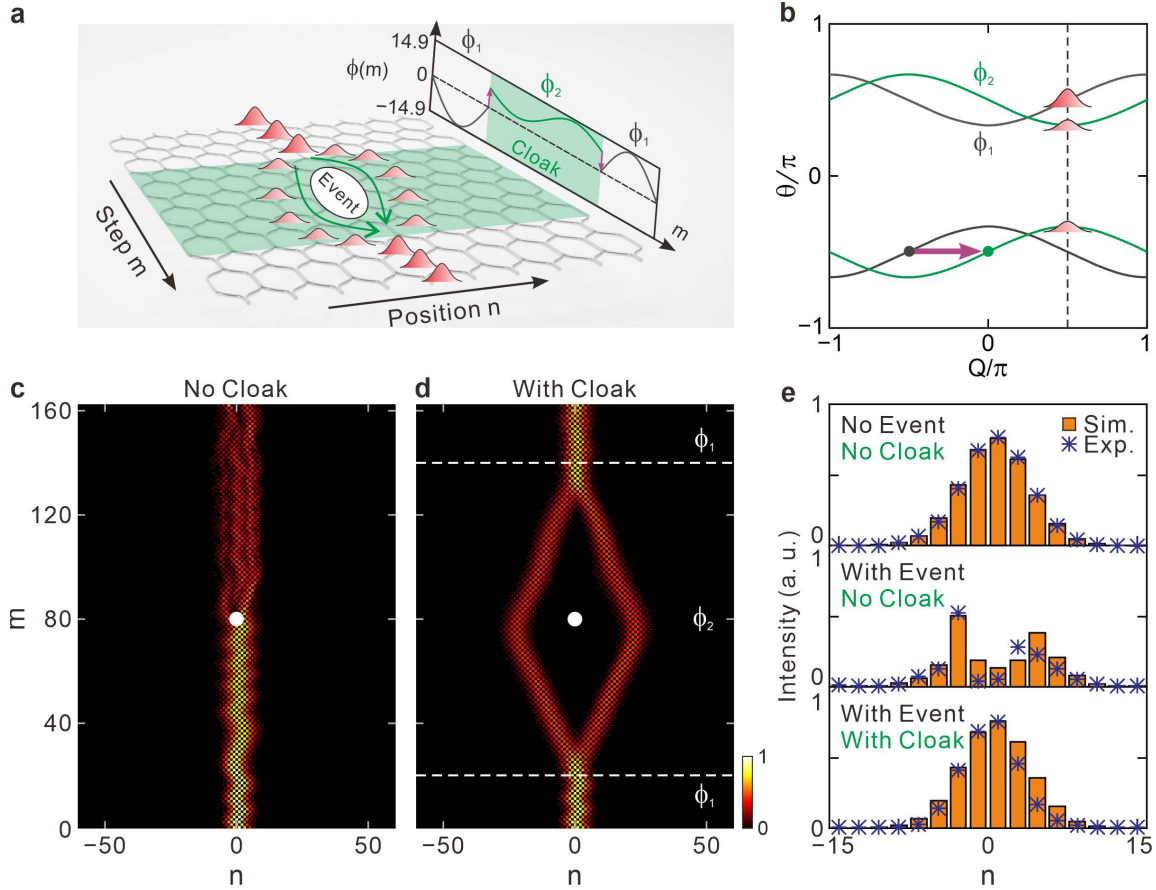


Fig. 5. Temporal cloaking with the combination of higher- and lower-order DLs. **a** Schematic of the temporal cloaking, where the green zone with modulation phase ϕ_2 denotes the cloak region and the gray zones with modulation phase ϕ_1 represent the regions outside the cloak. **b** Relative band structure shift for the two regions caused by abrupt change of the modulation phase. **c, d** Pulse intensity evolutions without and with the temporal cloak. The white point denotes the temporal absorption event. **e** Pulse intensity distribution sliced at $m = 162$. The orange blocks and blue asterisks represent the simulated and experimental results, respectively.

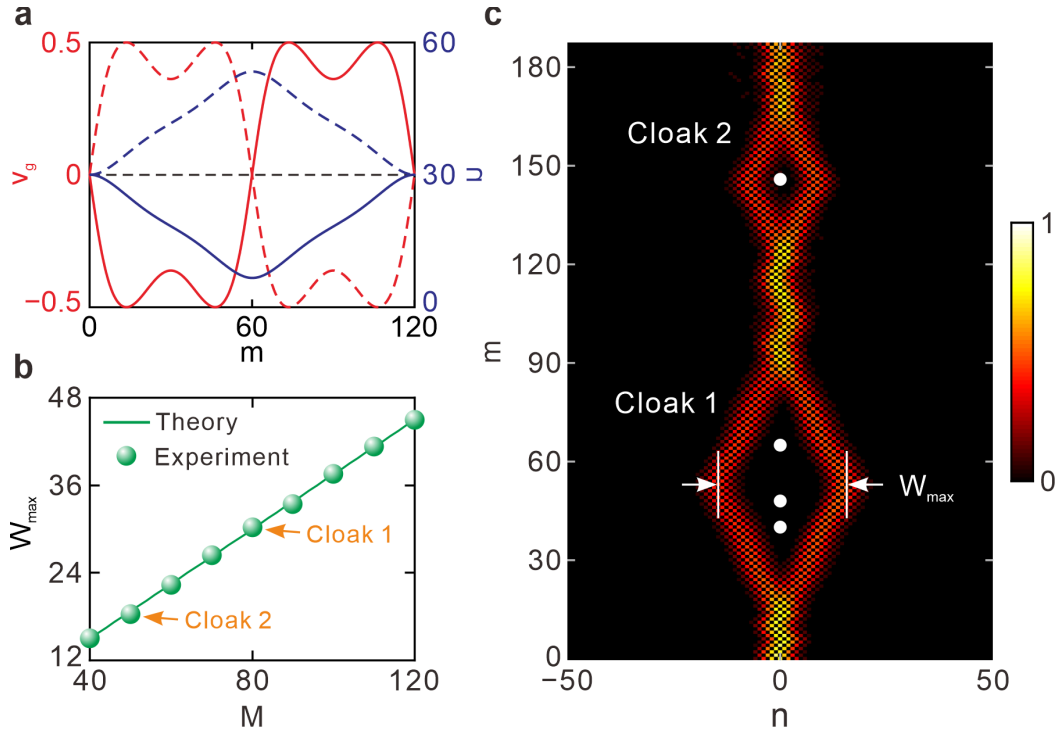


Fig. 6. Tunability of the cloak's window size and opening time. **a** Transverse group velocity v_g and displacement Δn with respect to step m . The dashed and solid curves correspond to the lower and upper bands, respectively. **b** Cloak width W_{\max} varying with driving period M . **c** Measured pulse intensity evolution with two cloaks. For cloak 1 and 2, the corresponding driving periods are $M = 80$ and $M = 50$, respectively.

Supplementary Files

This is a list of supplementary files associated with this preprint. Click to download.

- [SupplementaryMaterials.pdf](#)